CellPress

Structure
Article

Molecular Basis of Substrate Recognition and Degradation by Human Presequence Protease

John V. King,[1,5] Wenguang G. Liang,[1] Kathryn P. Scherpelz,[2] Alexander B. Schilling,[3] Stephen C. Meredith,[4] and Wei-Jen Tang[1,*]

[1]Ben May Department for Cancer Research, The University of Chicago, 929 E. 57th Street, Chicago, IL 60637, USA
[2]Department of Biochemistry and Molecular Biophysics, The University of Chicago, Chicago, IL 60637, USA
[3]Mass Spectrometry, Metabolomics, and Proteomics Facility, University of Illinois at Chicago, Chicago, IL 60612, USA
[4]Department of Pathology, The University of Chicago, Chicago, IL 60637, USA
[5]Present Address: Neuroscience Graduate Program, University of California San Francisco, San Francisco, CA 94158, USA
*Correspondence: wtang@uchicago.edu
http://dx.doi.org/10.1016/j.str.2014.05.003

SUMMARY

Human presequence protease (hPreP) is an M16 metalloprotease localized in mitochondria. There, hPreP facilitates proteostasis by utilizing an ~13,300-Å^3 catalytic chamber to degrade a diverse array of potentially toxic peptides, including mitochondrial presequences and β-amyloid (Aβ), the latter of which contributes to Alzheimer disease pathogenesis. Here, we report crystal structures for hPreP alone and in complex with Aβ, which show that hPreP uses size exclusion and charge complementation for substrate recognition. These structures also reveal hPreP-specific features that permit a diverse array of peptides, with distinct distributions of charged and hydrophobic residues, to be specifically captured, cleaved, and have their amyloidogenic features destroyed. SAXS analysis demonstrates that hPreP in solution exists in dynamic equilibrium between closed and open states, with the former being preferred. Furthermore, Aβ binding induces the closed state and hPreP dimerization. Together, these data reveal the molecular basis for flexible yet specific substrate recognition and degradation by hPreP.

INTRODUCTION

Throughout all domains of life, regulated proteolysis ameliorates the effects of protein damage, misfolding, and aggregation (Powers et al., 2009). Unlike canonical protein-protease networks, M16 metalloproteases, which are Zn^{2+}-dependent and ATP-independent, do not select substrates on the basis of posttranslational modifications or embedded degradation tags (Malito et al., 2008; Ravid and Hochstrasser, 2008; Sauer and Baker, 2011). These proteases are vital to an array of biological processes, including the clearance of insulin and other peptide hormones by human *i*nsulin-*d*egrading *e*nzyme (IDE) (Guo et al., 2010), the removal of targeting peptides from preproteins by the *m*itochondrial *p*rocessing *p*eptidase (MPP, also a component of the cytochrome bc1 complex in plants) (Taylor et al., 2001; Xia et al., 1997), and the catabolism of hemoglobin by *fal*cilys*in* (Fln) in the malaria parasite (Murata and Goldberg, 2003). Structural studies revealed that M16 proteases share a conserved architecture of two homologous, ~50-kDa domains enclosing a large catalytic chamber. Three families, M16A–C, have been characterized on the basis of the connection between these two domains. In M16A, a short loop connects the two domains (Shen et al., 2006), whereas an extended helical linker joins them in M16C (Johnson et al., 2006). M16B proteases lack a linker because the two subunits arise from distinct genes (Taylor et al., 2001) (Figure 1A). Because several M16 substrates, e.g. insulin and amyloid-β (Aβ), are involved in the pathogenesis of human disease, dissecting the operating logic of M16 proteases has been a subject of numerous investigations (Falkevall et al., 2006; Manolopoulou et al., 2009).

*H*uman *p*resequence *p*rotease (hPreP) is a 117-kDa M16C enzyme that is widely expressed in human tissues (Mzhavia et al., 1999). HPreP primarily localizes to the mitochondrial matrix, where it cuts an array of peptides into recyclable fragments (Alikhani et al., 2011a; Chow et al., 2009; Falkevall et al., 2006). Its substrates include N-terminal mitochondrial targeting peptides or presequences, the clearance of which is vital to proteostasis because these peptides can insert into mitochondrial membranes, disrupting their electrical potential and uncoupling respiration (Koppen and Langer, 2007; Mossmann et al., 2012). Consistent with this idea, double knockout of *A. thaliana* PreP (atPreP) 1 and 2 results in a delayed growth phenotype, whereas yeast PreP deletions display impaired growth on a nonfermentable carbon source under aerobic conditions (Kambacheld et al., 2005; Nilsson Cederholm et al., 2009). Substrate recognition and degradation by PrePs is modeled from the closed-state structure of atPreP, which uses a negatively charged catalytic chamber to engulf substrate peptides of up to ~65 residues while excluding larger, folded proteins (Falkevall et al., 2006; Johnson et al., 2006; Ståhl et al., 2005). Within the chamber, a copurified peptide was observed, revealing that catalysis requires the close apposition of conserved residues on both the N and C domains. In the closed state, substrates cannot enter the catalytic chamber, and reaction products cannot exit. However, the nature of the conformational switch(es) that PrePs undergo to permit substrate capture is not well understood. HPreP's architecture is expected to be similar to atPreP based

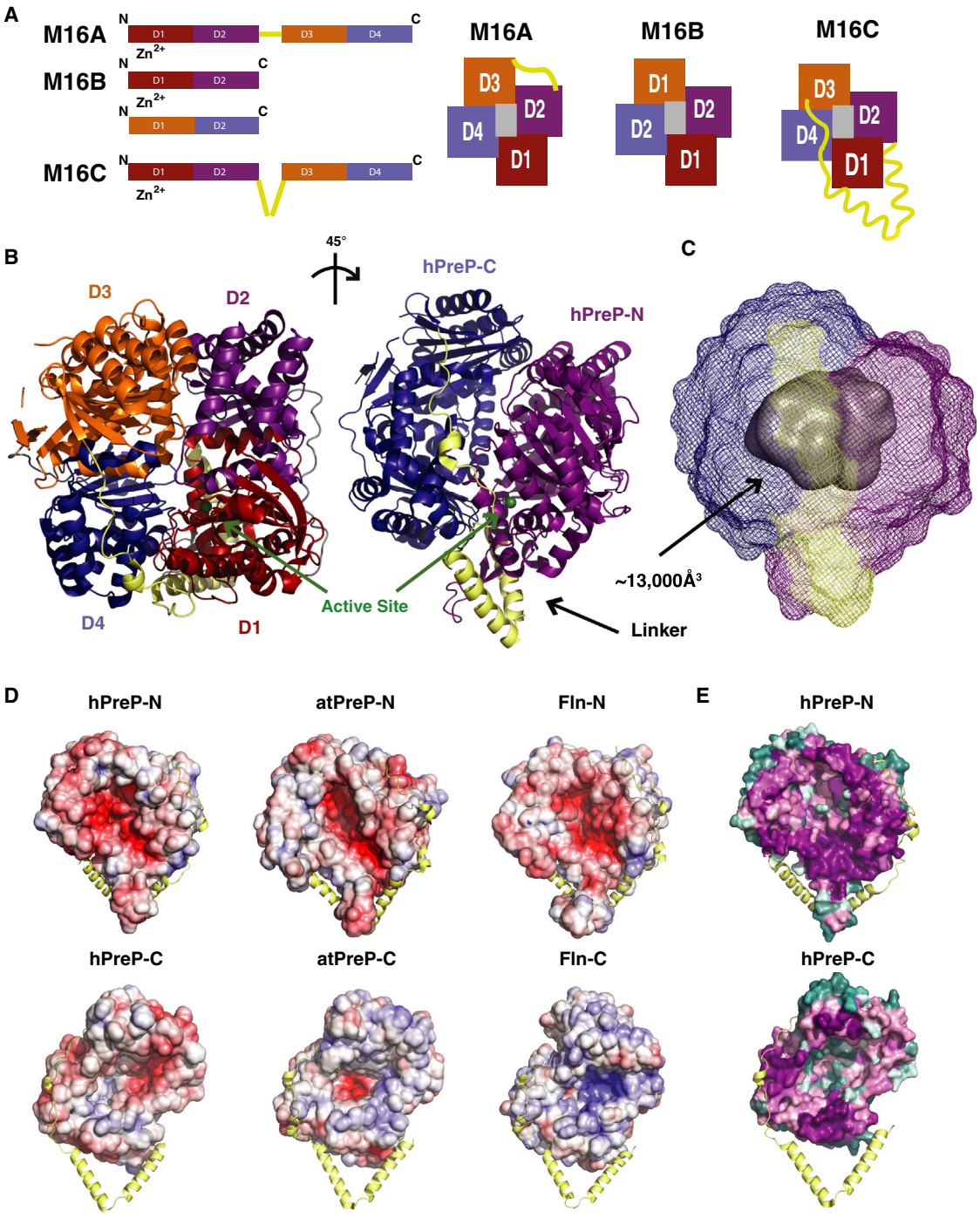

Figure 1. Conserved Mechanisms for Substrate Capture by hPreP

(A) M16 metalloprotease domain organization.

(B) Crystal structure of hPreP.

(C) Volumetric analysis of the hPreP catalytic chamber performed with 3V (Voss and Gerstein, 2010).

(D) Electrostatic surface representations of the hPreP, atPreP (Protein Data Bank ID code 2FGE), and Fln (PDB ID code 3S5H) catalytic chambers at ± 6 kT/e performed with APBS (Baker et al., 2001). Positive surfaces are blue, negative ones red, and neutral ones white.

(E) Analysis of M16C catalytic chamber conservation performed with ConSurf (Ashkenazy et al., 2010). Positions are colored on a sliding scale from magenta (most conserved) to teal (degenerate).

See also Figures S1 and S2.

Table 1. Data Collection and Refinement Statistics

Crystal	hPreP E107Q	hPreP E107Q + $A\beta_{40}$
PDB ID code	4L3T	4NGE
Data Collection		
Beamline	APS 19ID	APS 19ID
Wavelength (Å)	0.97895	1.045
Space group	C2	C2
Unit Cell Parameters		
a, b, c (Å)	245.8, 85.1, 158.5	247.3, 86.2, 158.6
α, β, γ (°)	90, 127.5, 90	90, 127.6, 90
Molecules in ASU	2	2
Resolution (Å)	50–2.03	50–2.70
R_{sym} (%)[a]	8.6 (58.5)[b]	18.0 (59.7)
I/σ	17.1 (2.8)	8.59 (1.8)
Redundancy[c]	4.1 (3.8)	2.9 (2.4)
Completeness	98.2 (97.0)	99.1 (98.2)
Unique reflections	163,827 (8,053)	71,876 (3,557)
Heavy atom sites	54	5
Figure of merit	0.83	0.82
Refinement		
R_{work} (%)[d]	17.1	19.1
R_{free} (%)[e]	21.0	23.2
RMS Deviations		
Bond lengths (Å)	0.012	0.004
Bond angles (°)	0.99	0.85
Number of		
Protein atoms	15,892	15,986
Solvent molecules	1154	68
Metal cofactors	2	2
Ramachandran plot (%)		
Preferred region	98.17	97.09
Allowed region	1.83	2.91
Disallowed region	0	0
B-factors (Å^2)		
Protein	35.3	44.5
Solvent	46.4	49.6

[a] $R_{sym} = \Sigma_j | < I > - I_j | \Sigma < I >$, where I_j is the intensity of the j^{th} reflection and $< I >$ is the average intensity.
[b] Values in parentheses indicate the outer resolution shell.
[c] N_{obs}/N_{unique}.
[d] $R_{work} = \Sigma_{hkl} | F_{obs} - F_{calc} | / \Sigma_{hkl} | F_{obs} |$.
[e] R_{free} calculated as R_{work} but on 5% data excluded from refinement.

on 27% sequence identity. However, hPreP functions in radically different biological contexts from atPreP and, correspondingly, has distinct substrate cleavage patterns. Thus, hPreP likely employs a distinct set of substrate recognition and degradation principles (Chow et al., 2009; Johnson et al., 2006; Malito et al., 2008).

Intriguingly, hPreP degrades several functionally relevant Aβ species ($A\beta_{40}$, $A\beta_{42}$, and $A\beta_{Arctic}$) that are generated by β- and γ-secretase cleavage of the amyloid precursor protein (Falkevall et al., 2006). Aβ aggregates are toxic to the neuron and play a key role in Alzheimer's disease (AD) pathogenesis through intra- and extracellular signaling pathways. Mutations in Aβ production pathways, e.g. at γ-secretase and amyloid precursor protein loci, can lead to Aβ accumulation and familial AD (Huang and Mucke, 2012; Yankner and Lu, 2009). Defects in Aβ clearance pathways may be important to both familial and sporadic or late-onset AD (Malito et al., 2008; Saido and Leissring, 2012). Joint action of proteases, including IDE, neprilysin, and cathepsin B, clears Aβ from the extracellular matrix, cytosol, ER, Golgi, endosomes, and lysosomes (Farris et al., 2003; Iwata et al., 2001; Mueller-Steiner et al., 2006). Recent studies indicate that hPreP is the Aβ-degrading protease in mitochondria (Alikhani et al., 2011b; Falkevall et al., 2006; Pinho et al., 2010). Immunodepletion of hPreP in human brain mitochondria prevents degradation of mitochondrial Aβ. Additionally, hPreP activity is diminished in AD brains compared with age-matched controls. Mitochondrial lesions are implicated in AD pathogenesis, and mitochondria may be sites of Aβ accumulation and toxicity through inhibition of Aβ-binding alcohol dehydrogenase and increased production of reactive oxygen species (Lustbader et al., 2004; Manczak et al., 2006). These data suggest that a molecular appreciation of hPreP's operating logic can increase our understanding of AD pathogenesis.

Although IDE uses its catalytic chamber to specifically recognize and cleave amyloidogenic peptides, the molecular basis for Aβ destruction by hPreP remains elusive. Here we describe the crystal structure of hPreP, which reveals that size exclusion and charge complementation are key principles for substrate capture and identifies those residues within the catalytic chamber used for recognition of diverse peptide motifs. We further show that the dynamics of substrate capture are modulated by the enzyme's linker region. Crystallographic and mass spectrometry (MS) analyses reveal how hPreP specifically binds Aβ by relaxing the requirement for a defined orientation of the peptide in the catalytic cleft and using both a hydrophobic exosite and S1 pocket to recognize and degrade Aβ in a selective, nonprocessive manner. Finally, small-angle X-ray scattering (SAXS) analysis reveals the nature of the closed-to-open conformational switch that permits substrate entry into the catalytic chamber and shows that substrate binding can induce domain closure and dimerization. Together, these data reveal the mechanisms hPreP employs for recognition and degradation of amyloidogenic peptides.

RESULTS AND DISCUSSION

Crystal Structure of hPreP

To elucidate the molecular basis for hPreP substrate recognition, we determined the crystal structure for isoform 1 of substrate-free hPreP in a closed conformation at 2.0 Å (Figure 1B; Table 1). Two key modifications were required to obtain diffracting crystals: surface lysine methylation, which reduced catalytic activity but did not impact protein purity, and introduction of an active site E107Q substitution, which renders hPreP catalytically inactive but substrate-binding competent (Figure S1 available online) (Johnson et al., 2006; Rypniewski et al., 1993). Iodine-based single-wavelength anomalous dispersion (SAD) phases were crucial for removing the phase bias of the initial molecular replacement (MR) solution and drastically improved the electron density map in key regions, e.g. the hPreP linker, that were

otherwise disordered (Figure S2) (Abendroth et al., 2011). Displaying an overall architecture that is highly conserved across the M16C family, hPreP is composed of the hPreP-N (amino acids [aa] 33–509) and hPreP-C (aa 576–1037) domains, which are connected by an extended helical hairpin (aa 510–575). HPreP-N and hPreP-C can be further broken down into topologically similar D1–D4 (Figure 1B). Although D1–D4 superimpose poorly onto one another, pairs D1 (aa 33–288) and D3 (aa 576–844) (root-mean-square deviation [rmsd] = 3.9 Å for 862 atom pairs) and D1 and D4 (aa 855–1037) (rmsd = 4.2 Å for 732 atom pairs) superimpose best onto one another. The other four pairwise comparisons yield rmsds greater than 5.1 Å. This is consistent with ancient gene duplication that used D1 as a template for hPreP-C.

The hPreP structure demonstrates that substrate selection by size exclusion is a conserved mechanism of M16C proteases. HPreP-N and HPreP-C enclose a large, ~13,300-$Å^3$ chamber for engulfing substrates (Figure 1C). Formation of the active site requires the close apposition of hPreP-N and HpreP-C, whereby the inverted zinc-binding motif on D1 (H_{104}XXEH…E_{205}) and residues R900 and Y906 on D4 form a cleft within the chamber for substrate binding and catalysis (Figure S2) (Johnson et al., 2006). Because there is no portal for substrate access in this conformation, substrates too large to fit into the enclosed chamber are excluded on the basis of their size. Available M16C structures, atPreP and Fln, have similarly sized chambers (~13,000 $Å^3$ and ~12,500 $Å^3$, respectively), indicating that the upper limit for substrate size determined for atPreP, ~65 residues, is conserved across species (Figure S2) (Moberg et al., 2003; Ståhl et al., 2005).

Electrostatic interactions play a key role in M16 substrate capture (Johnson et al., 2006; Manolopoulou et al., 2009; Ralat et al., 2011). Interestingly, we observed that, although the N halves of M16C chambers are uniformly negatively charged, the C halves are variably charged between species (Figure 1D). The surface of Fln-C is mostly positively charged. HPreP-C has a weakly and variably charged surface, whereas atPreP-C contains a negatively charged pocket surrounded by a weakly positive surface. Furthermore, PreP-N is composed of highly conserved residues, whereas PreP-C is largely degenerate except for those residues that contribute to the catalytic cleft or form contacts with hPreP-N (Figure 1E). These data support a model for substrate selection by unipolar charge complementation between hPreP-N and substrates. The unique charge distribution in hPreP's catalytic chamber may explain why hPreP fails to degrade intact insulin because hPreP-C lacks a positively charged surface to trap negatively charged insulin in the chamber (Falkevall et al., 2006; Manolopoulou et al., 2009).

Topography of the Catalytic Chamber

Characteristics of the hPreP catalytic chamber provide a structural basis for the protease's observed substrate degradation patterns (Figure 2A) (Chow et al., 2009). The hPreP-N chamber contains two deep pockets near the active site (Figure 2B). A hydrophobic pocket, consisting of L111, F123, F124, and L127, forms an S_1 or S'_1 site immediately adjacent to the active site, which explains the preference for bulky hydrophobic residues immediately adjacent to the scissile bond. A second, basic pocket comprised of R888 and H896, 12–16 Å away from the catalytic zinc, can bind substrate C termini via salt bridges (Figure 2B). The existence of these pockets explains why cleavage sites with hydrophobic residues in the P_1 or P'_1 positions can be found two to five residues from the C terminus (Chow et al., 2009; Falkevall et al., 2006). Furthermore, this explains why, despite a high degree of architectural similarity (Figure S2), hPreP has distinct substrate preferences from atPreP, which uses an acidic S'_1 pocket to bind basic residues in the P'_1 position (Johnson et al., 2006; Ståhl et al., 2005). These features of hPreP's catalytic cleft may also explain how hPreP effectively degrades peptides as small as leu-enkephalin, a pentapeptide, whereas the minimal substrate length for atPreP is proposed to be 11 residues (Chow et al., 2009; Ståhl et al., 2005).

Presequences are diverse in sequence but have similar physiochemical properties in that they are enriched in positively charged and hydrophobic residues segregated on opposite faces of amphipathic α helices (Moberg et al., 2004). In the hPreP chamber, residues D716, D212, E214, and D377 form a contiguous, negatively charged surface 15–19 Å away from the active site (Figure 2C). Not only would these residues contribute to attracting positively charged residues in presequences, but their arrangement also explains why hPreP prefers arginines three to five residues distal to the scissile bond (Chow et al., 2009). Hydrophobic clusters are also present inside the hPreP-N chamber. These include those formed by L60, F443, M446, and L447; by Y380, Y383, and Y450; and by F344, L348, L428, and I432 (Figure 2D). The presence of these residues suggests that hydrophobic surfaces facilitate the recognition of substrates diverse with respect to the precise location of hydrophobic residues.

Mutational Analysis of the Linker Region

An extended helical hairpin, originating in D2 and stretching across the surface of hPreP to terminate in D3, is the distinguishing structural feature of the M16C family (Figures 1A and 1B). The importance of the linker for catalytic efficacy and allostery of IDE, an M16A enzyme, is documented (McCord et al., 2013). The PreP linker is likely involved in bringing PreP-N and PreP-C into close apposition for efficient catalysis (Johnson et al., 2006). To test this, we targeted P558 and L557. Both are highly conserved and rest in a conserved hydrophobic pocket on D1 (Figure 3A; Figure S3). We generated mutations to assess the importance of proline's restricted dihedral freedom (P558G) and of the hydrophobic pocket's integrity (L557E) to catalysis. We found that L557E and P558G exhibited ~20 and 40% the specific activity of WT hPreP, respectively (Figure 3B). Kinetic analysis revealed that both mutants have a reduced V_{max} and that L557E has an increased K_M (Figure 3C). A fluorescence thermal shift confirmed that these effects are specific to hPreP kinetics because mutants display melting curves and melting temperature (T_m) values similar to the wild type (WT), ruling out the possibility that mutants are simply destabilized (Figure S3). These findings support a role for the linker in catalytic competency, likely by modulating the open-closed conformational switch that is required for efficient catalysis.

MS Analysis of Aβ Degradation by hPreP

Using Aβ as a model substrate, we examined the sequence of cleavage events that follows substrate capture to resolve

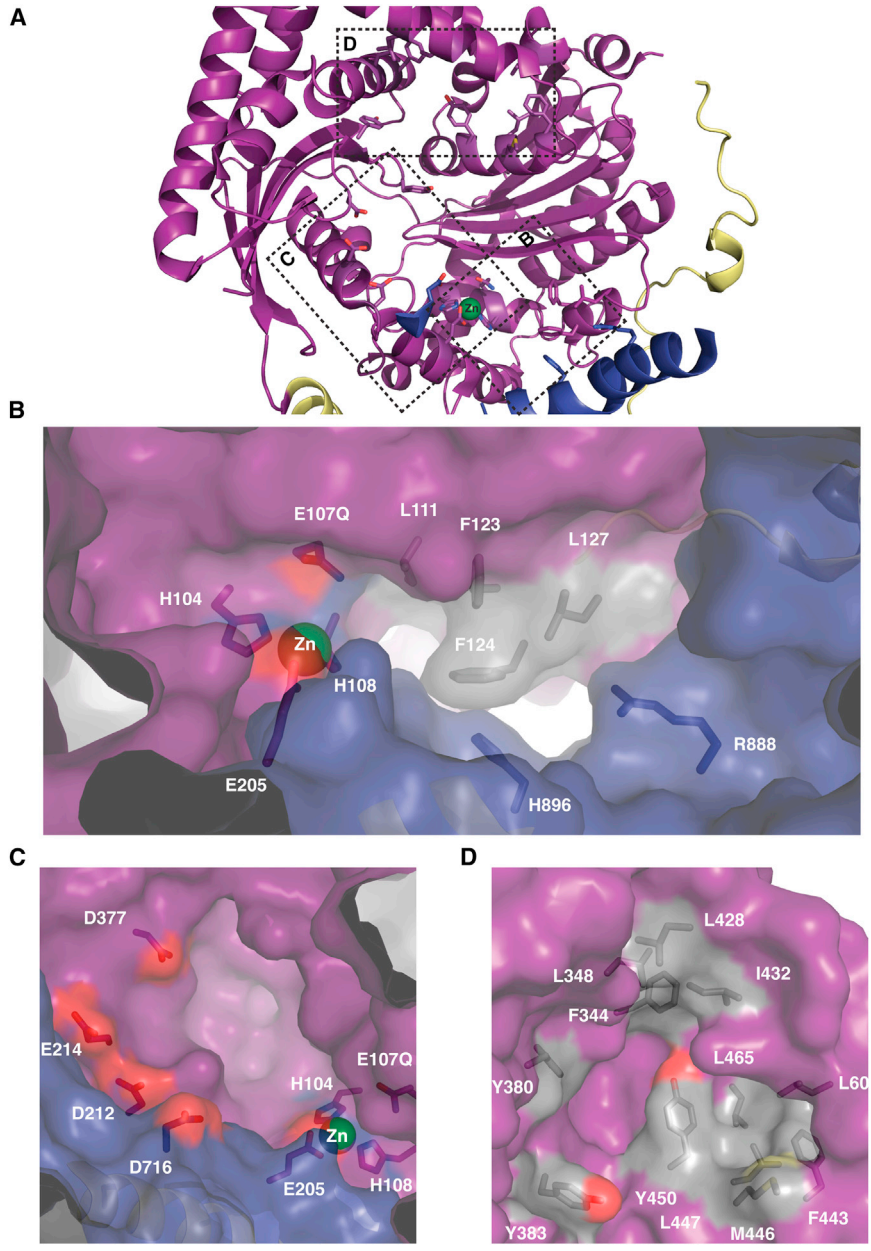

Figure 2. Residues in the hPreP Chamber Facilitate Substrate Recognition

(A) HPreP-N catalytic chamber.

(B) Two pockets (L111, F123, F124, and L127 as well as H896 and R888) explain the observed cleavage site preference for P_1 or P'_1 hydrophobic residues and scissile bonds two to five residues distal from substrate C termini.

(C) Labeled acidic residues are proximal to the active site and can facilitate interaction with basic substrate residues.

(D) A network of hydrophobic resides in hPreP-N permits the capture of hydrophobic residues.

whether hPreP degrades substrates stochastically and whether degradation proceeds along a defined path. Based on previous liquid chromatography-tandem mass spectrometry (LC-MS/MS) data, the cleavage sites of $A\beta_{40}$ by hPreP could occur after Q15, K16, F19, F20, A30, G33, and L34 (Falkevall et al., 2006). However, a separate study identified cleavage sites to be restricted to sites following F20 and L34 (Figure 4C) (Chow et al., 2009). Falkevall et al. (2006) used prolonged incubation (1 hr), whereas Chow et al. (2009) did not report precise experimental conditions. To discriminate full-length Aβ cleavage sites from those that arise from subsequent cleavages of reaction products, we quenched the Aβ degradation reaction rapidly (~1 s). Tandem mass spectrometry (MS/MS) analyses of the resultant $A\beta_{40}$ fragments using MALDI-TOF/TOF revealed that $A\beta_{1\text{-}20}$ is the single major cleavage product, increasing in abundance at higher hPreP concentrations (Figure 4A; Table 2). A secondary fragment, $A\beta_{1–19}$, became noticeable only at high hPreP concentrations. However, we could not detect the corresponding C-terminal Aβ fragments. We then turned to quadrupole TOF (Q-TOF) LC-MS/MS to ensure the comprehensive identification of degraded Aβ fragments with high mass accuracy. In these spectra, $A\beta_{1–20}$ and $A\beta_{21–40}$ are the dominant species observed and $A\beta_{20–40}$ the minor one (Figure 4B; Table 2; Figure S2). Thus, hPreP prefers to cut between F20 and A21, whereas cleavage between F19 and F20 is a secondary cut site, which reveals that Aβ degradation by hPreP is not a stochastic process. The fact that we did not observe most of the previously identified cleavage sites suggests that these are used after Aβ degradation products are available to serve as substrates (Figure 4C). From these data, we deduce that Aβ in the hPreP chamber is cleaved once and that the resulting products are subsequently released. Thus, hPreP degrades Aβ in a selective manner that is not processive.

We also used our MS data to estimate hPreP's catalytic efficiency. Previously, the k_{cat} for Aβ degradation was estimated at ~0.06 s^{-1}, with a K_M of ~2 μM, using Aβ as an alternate substrate inhibitor for a fluorescent peptide (Chow et al., 2009). Surprisingly, our Q-TOF data show that hPreP degrades $A\beta_{40}$ at a rate of ~300 s^{-1} (Figure 4B; Table S2). Our TOF-TOF data showed a similarly high rate, ~25–300 s^{-1} across different hPreP concentrations (Figure S4; Table S2). This rate is 2–3 orders of magnitude higher than reported previously (Chow et al., 2009), suggesting that hPreP is a highly efficient protease.

Structure of hPreP in Complex with Aβ

To elucidate the structural basis for specific hPreP recognition and degradation of Aβ, we determined the structure of the hPreP E107Q-$A\beta_{40}$ complex at 2.70 Å by MR/SAD using the arsenic

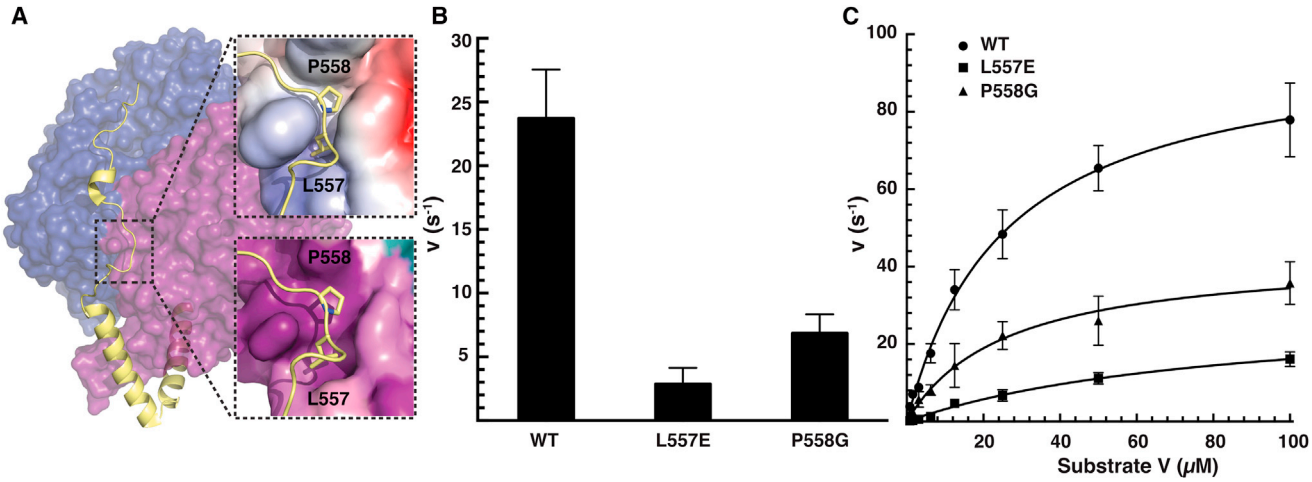

Figure 3. Role of the Linker in Catalysis

(A) L557E and P558G sit in a conserved hydrophobic pocket on the D1 surface. The lower inset is colored by the electrostatic surface and the upper one by conservation.

(B) Specific activities of hPreP WT and mutants at an enzyme concentration of 1.25 nM. Activity was determined by monitoring the cleavage of 0.5 μM substrate V at 37°C.

(C) WT and mutant hPreP specific activities at indicated substrate V concentrations. Data sets were fit to the Michaelis-Menten equation, with V_{max} (98, 29, 43 s^{-1}) and K_m (26, 82, 26 μM) calculated for WT, L557E, and P558G, respectively. Mean ± SD represents at least three experiments.

See also Figure S3.

moiety of cacodylated cysteines as the heavy atom (Table 1; Figure S2) (Dyda et al., 1994). Aβ, bound to the hPreP-N chamber (Figure 5A), was visible by inspection of the initial MR/SAD solution and omit maps (Figure S5). We observed two bulky side chains in the electron density immediately adjacent to the scissile bond that, as revealed by our mass spectrometry data, correspond to F19 and F20 (Figure 4; Figure S5). Based on this assignment, we built the remaining visible Aβ residues (Q15–D23), which produced a good fit for the observed density (Figure 5D). The geometry of the active site is such that the peptidyl bond between Aβ F20 and A21 is ideally positioned for hPreP's catalytic base E107—whose ε1 and ε2 oxygens would be 5.0 and 4.0 Å away, respectively, based on the position of Q107—to deprotonate a water molecule for nucleophilic attack on the scissile bond (Figure 5D) (Johnson et al., 2006; Shen et al., 2006).

HPreP uses a trio of structural features to recognize Aβ in the catalytic cleft. First, hPreP binds Aβ in an orientation opposite to those observed previously in substrate-bound M16 structures (Figure 5C) (Johnson et al., 2006; Shen et al., 2006; Taylor et al., 2001). The relaxed requirement for substrate orientation in the cleft demonstrates an unexpected degree of flexibility in the manner in which hPreP binds substrates. Second, hydrophobic interactions coordinate substrates in the active site. A hydrophobic pocket formed by L111, F123, and F124 forms a highly conserved S1 site for Aβ F20 in the P1 position (Figures 1E, 5C, and 5D). Interestingly, hPreP repurposes R900 and Y906, which were found to coordinate atPreP substrate backbone carbonyls and are required for efficient catalysis (Johnson et al., 2006). R900 completes the S1 site through a cation-π interaction with Aβ F20, whereas Y906 forms a hydrogen bond with F20's backbone amine (Figures 5C and 5D). Finally, hPreP uses a β strand (β7) to coordinate Aβ in the cleft in a manner that specifically impairs Aβ's ability to aggregate (Figure 5C). Although Aβ monomers are largely unstructured, structures of Aβ fibrils seeded from synthetic and human sources show that formation of parallel, intermolecular β sheets involves the same amyloidogenic segment of Aβ, KVLFF, that we observe binding to the hPreP catalytic cleft (Balbach et al., 2000; Lu et al., 2013; Paravastu et al., 2008; Tjernberg et al., 1996). Thus, the Aβ-bound hPreP structure reveals that hPreP is specialized to recognize and cleave the amyloidogenic segment of Aβ that is prone to form β sheets, thereby preventing Aβ aggregation in mitochondria.

Interestingly, we observed four unknown Aβ residues binding to a pocket on hPreP-N in both the MR/SAD solution and composite omit maps (Figure 5A; Figure S5). We were unable to resolve these residues' side chains, which indicates that this site anchors multiple Aβ segments. The first of these residues (x_1) is separated by 9.5 Å (approximately three residues) from the N terminus of the remaining three residues ($y_{1–3}$) (Figure 5B). A single bulky side chain is visible in the electron density protruding from y_1 (Figure 5E), which is consistent with binding of bulky hydrophobic residues from either the Aβ N or C terminus (Figure 4C). Based on this area's enrichment in hydrophobic residues (specifically L348, L428, I432, and F344 and L465, L60, F443, L447, and Y450) and the presumptive orientation of the Aβ side chains toward them, we term it the "hydrophobic exosite." This site is likely an evolutionarily recent development because its conservation is relatively weak (Figure 1E). We propose that the hPreP exosite plays a role in anchoring larger peptides (≥~40 residues) in the chamber, enabling their efficient degradation (Manolopoulou et al., 2009; Ralat et al., 2011). This hydrophobic clamp would confine the interaction of Aβ with hPreP, explaining why the primary cleavage site is between $Aβ_{20}$ and $Aβ_{21}$. The existence of this site also offers an explanation for how hPreP is able to efficiently capture Aβ despite Aβ

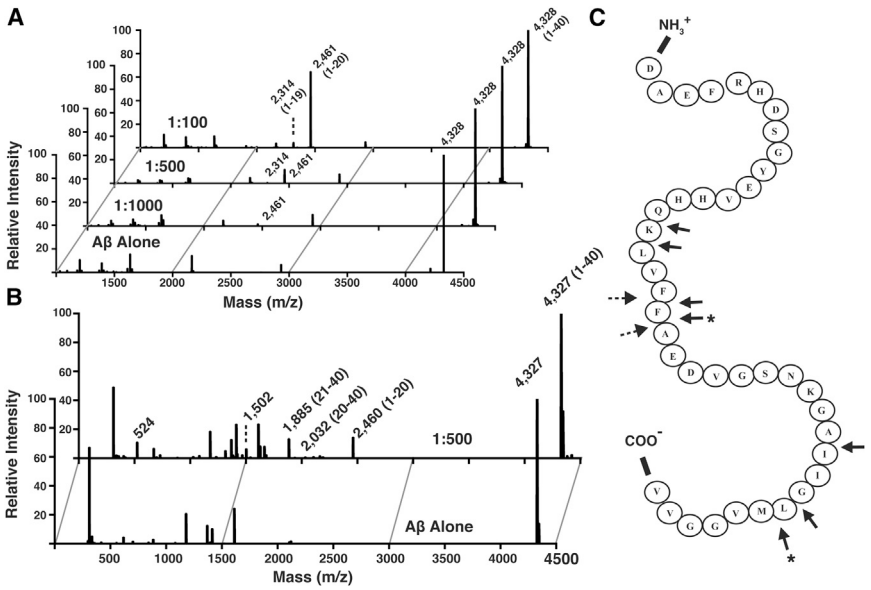

Figure 4. Mass Analysis of Aβ Degradation by hPreP

(A and B) MALDI-TOF/TOF (A) and deconvoluted Q-TOF mass spectra (B) of $A\beta_{40}$ alone (lower panel) and hPreP-degraded $A\beta_{40}$ (upper panels). $A\beta_{40}$ and hPreP were mixed at the indicated molar ratios (1:100–1000).

(C) Schematic of hPreP's $A\beta_{40}$ cleavage sites. Filled arrows denote sites identified by Falkevall et al. (2006), whereas dashed arrows indicate cleavage sites identified in this study. Asterisks mark cleavage sites reported by Chow et al. (2009).

See also Figure S4.

carrying a net negative charge (isoelectric point [PI] = 5.4) in the mitochondrial matrix (pH ~7.8) that would otherwise be repelled by hPreP-N (Porcelli et al., 2005).

Conformational Profile of hPreP in Solution

To identify the nature of the conformational switch that permits substrate capture and assess the effect of substrate binding on hPreP dynamics, we analyzed the conformational states of hPreP in solution with SAXS. The observed radius of gyration (R_g) and maximum diameter (D_{max}) (33 and 117 Å, respectively) for WT hPreP were inconsistent with the parameters predicted for a population of closed-state monomers (R_g = 31 Å, D_{max} = 108 Å) or dimers (R_g = 46 Å, D_{max} = 149 Å) (Figures 6A and 6B). These findings agreed with the poor fit of theoretical scattering curves for closed monomers (χ = 3.2) and dimers (χ = 18.6) to the experimental data and the lack of intensity dip between 0.09–0.15 $Å^{-1}$. Analysis of the hPreP E107Q yielded similar results (Figures 6C and 6D), and we conclude that hPreP does not exist exclusively as a closed monomer or dimer in solution.

To directly assess the likelihood that hPreP populates multiple states in solution, we modeled open hPreP conformations, systematically increasing the displacement between hPreP-N and hPreP-C from 20 to 50 Å, and assessed their ability to account for the experimental data. We tested the "parallel spring," "hinge" (a D1/D4 pivot resembling the motion seen in M16A pitrilysin), and "Open Book" (a D2/D3 pivot resembling the motion seen in M16B MPP) motions (Figure S6) but found that no single open state yielded a good fit (χ < 2.0) to the data. We found that the hinge motions reliably produced better fits to the data than other types of motion with equivalent degrees of opening (Figure S6). By testing mixtures of closed monomers, dimers, and 20- to 50-Å hinge models, we were able to generate an excellent fit to the WT data (χ = 0.73), whose fractional occupancy consisted of ~72% closed monomers, ~8% closed dimers, ~20% 40-Å hinges (Figures 6A and 6B; Figure S6). A similar combination of states yielded the line of best fit for the E107Q mutant, but we observed a higher propensity for closed or partially closed states (Figures 6C and 6D). Together, these data reveal that hPreP is predominantly a closed monomer, which is consistent with our size exclusion data, with at least one open state in solution (Figure S1). Given the resolution limit for SAXS and the similarity of scattering curves for the 20-Å parallel spring, hinge, and open book (Figure S6) motions, the precise nature of the movements underlying the open state(s) of hPreP and their role in the hPreP catalytic cycle remain to be determined.

We next assessed whether substrate binding could modify the equilibrium between open and closed hPreP states in solution.

Table 2. TOF-TOF and Q-TOF Mass Spectrometry Analysis of hPreP-degraded Aβ[a]

TOF-TOF				
Aβ	M_{obs}[b]	M_{calc}[b]	Error[c]	b/y Ions
1–40	4,328.7	4,328.2	−0.5	N/A
1–20	2,461.4	2,461.2	−0.3	b5–9,b11–16, b18,b19,y7, y8,y10,y12–20
1–19	2,314.4	2,314.1	−0.3	b5–b8,b10–16, b18,y6,y7, y11–19
Q-TOF				
Aβ	M_{obs}	M_{calc}	Error[d]	b/y Ions
1–40	4,327.117	4,327.148	−7	b2,b6,b7,b9,b13–b15,b17, b20–b27,b30–b35,b38, y1–y6,y8–y9,y11,y18–y20, y23–y25,y28–y33
1–20	2,460.094	2,460.161	−27	b2,b5–b13,b15–b19, y1–y3, y5,y7–y14,y17–y18
20–40	2,032.032	2,032.066	−17	b2-b3,b5,b11–b20, y1–y2, y6–y7,y9–y21
21–40	1,884.989	1,884.998	−5	b2-b19,y1–y2,y3–y9, y11–y16,y18–y20

[a]Outside $A\beta_{1–40}$, peaks that exist in Aβ alone are not listed. Peaks that match predicted Aβ fragments but cannot be confirmed by MS/MS are listed in Table S1.
[b]$[M+H]^+$.
[c]Error (in Da).
[d]Error (in ppm) = $((M_{obs} - M_{calc}) / M_{calc})(10^6)$.

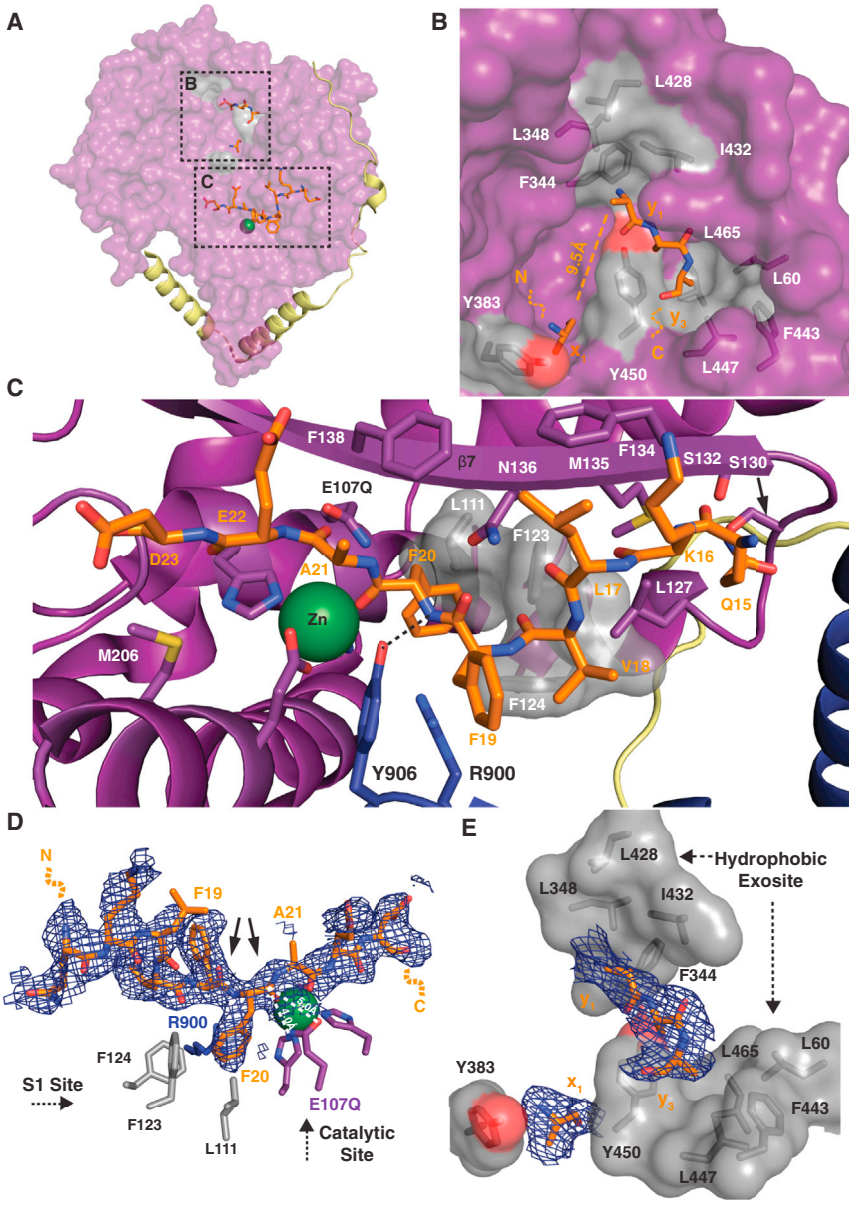

Figure 5. Structural Basis of Aβ Capture and Recognition by HPreP

(A) Aβ binding to hPreP-N.

(B) Hydrophobic exosite. Four Aβ residues (x_1 and y_{1-3}) are observed. Hydrophobic residues that comprise the putative side chain binding pockets are displayed in gray.

(C) Aβ binding to the hPreP catalytic cleft. The S1 site consists of L111, F123, F124, and R900.

(D and E) $2F_o$–F_c electron density maps contoured at 0.5 σ for Aβ residues bound to the catalytic cleft (D) and the hydrophobic exosite (E). Arrows denote preferred Aβ cleavage sites by hPreP.

See also Figure S5.

Comparison of hPreP and IDE

Although hPreP and IDE belong to distinct M16 families, they have been considered to be of the same functional class in terms of their ability to recognize and degrade amyloidogenic peptides (Aleshin et al., 2009). The structures of hPreP alone and in complex with Aβ confirm that hPreP and IDE both select substrates on the basis of their size, shape, and charge distribution. Furthermore, both hPreP and IDE target Aβ amyloidogenicity for destruction. However, the mechanism for Aβ degradation by hPreP is dramatically different from IDE. This difference may be due to the distinct nature of their exosites. The hPreP exosite recognizes a hydrophobic patch of Aβ or other substrate and acts in concert with the catalytic cleft to constrain cleavage sites. The hydrophobic exosite likely binds unfolded peptide segments because folded proteins usually do not present flexible, hydrophobic surfaces for capture. This would explain why hPreP prefers to degrade structurally disordered peptides (Falkevall et al., 2006). Consequently, hPreP preferentially cuts Aβ at a specific site nonprocessively. By comparison, the IDE exosite anchors substrate N termini via hydrogen bonds. This enables IDE substrates such as insulin, TGF-α, and MIP-1α to retain a defined tertiary structure within the chamber after capture. Because the unfolding of these proteins within the IDE chamber is required to stabilize the catalytic cleft, the cleavage of these peptides occurs stochastically at a few predefined sites, and cleavage proceeds processively (Guo et al., 2010; Manolopoulou et al., 2009; McCord et al., 2013; Ren et al., 2010). Our data also indicate that hPreP is 2- to 3-fold more efficient than IDE based on the measured specific activities of ~20 s^{-1} versus 10 s^{-1} for substrate V and ~25 s^{-1} versus 8 s^{-1} for Aβ (Figure 3B) (Im et al., 2007; McCord et al., 2013). This points toward the utility of both hPreP and IDE as targets for controlling the Aβ load in AD patients. Finally, the oligomerization and conformations of these two enzymes are distinct. HPreP is predominately

Analysis of the scattering curve for the hPreP E107Q-$Aβ_{40}$ complex revealed that the best fit to the data could be obtained using a combination of monomers (83%) and dimers (17%) exclusively in the closed state (χ = 1.3) (Figures 6E and 6F; Figure S6). The fit could not be improved with the addition of "open" states (Figure S6). The fraction of dimers observed in the substrate-bound solution doubled compared with the WT, showing that substrate binding can induce hPreP dimerization (Figures 6B and 6F). These results agreed with the appearance of an intensity dip from 0.09–0.15$Å^{-1}$ in the experimental data (Figure 6F). Together with the finding that domain closure occurs in the absence of substrate (Figures 1B, 6A, and 6B), these results show that substrate binding is sufficient, but not necessary, to induce domain closure, the consequence of which is to lock the enzyme in a catalytically competent state (Aleshin et al., 2009; Johnson et al., 2006).

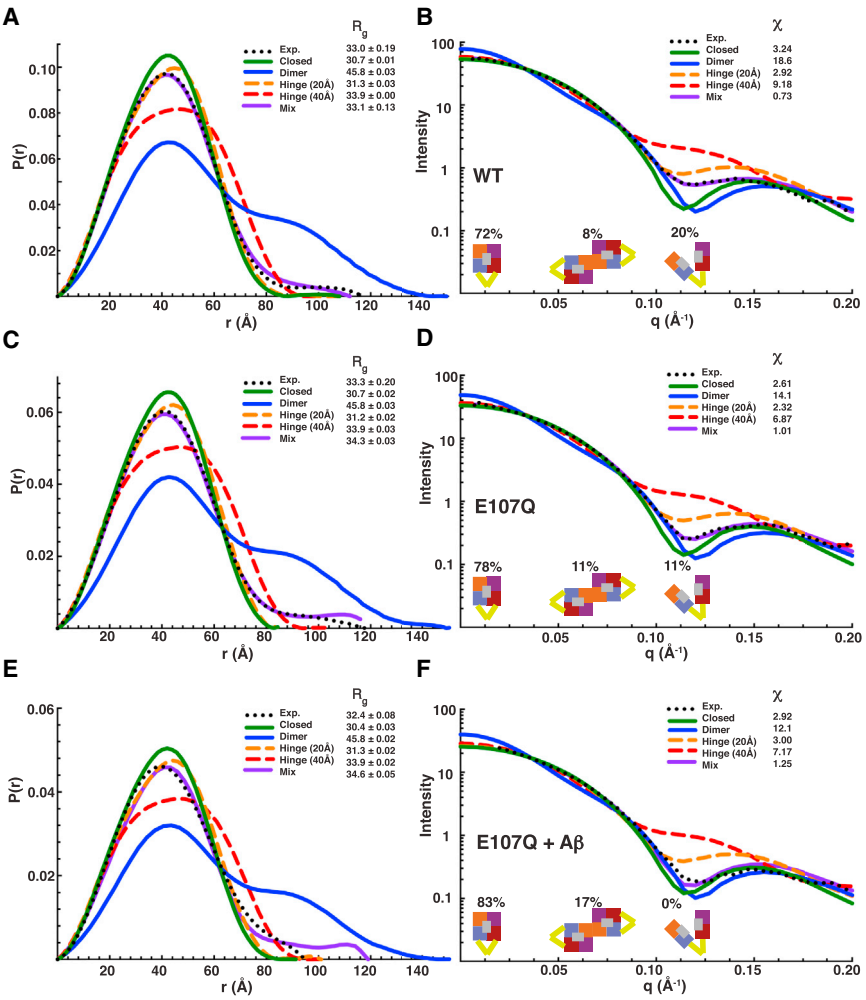

Figure 6. Conformational Profiles of hPreP in Solution

Pair distribution functions and scattering curves for WT (A and B), E107Q (C and D), and E107Q and Aβ (E and F). Curve fitting was performed based on atomic model input to CRYSOL (single models) and OLIGOMER (multiple models). The volume fractions shown below the profiles indicate the percent composition by the conformational state in solution that yielded the line of best fit for the observed data (mixture). Exp., experimental.

See also Figure S6.

monomeric and closed, whereas IDE is a dimer that predominantly occupies open states in solution (McCord et al., 2013). Thus, hPreP and IDE likely target distinct sets of substrates in vivo, and hPreP should not be considered to be mitochondrial IDE.

Conclusions

The biology of hPreP is poorly understood. However, high-throughput proteomics approaches indicate that hPreP undergoes posttranslational modification by phosphorylation and participates in protein-protein interactions with key components of the citric acid cycle (Havugimana et al., 2012; Olsen et al., 2010), either or both of which could enhance the clearance of toxic peptides that impair mitochondrial function. Here we developed a molecular picture of hPreP substrate recognition and degradation that provides the structural context for future studies to unravel the roles of hPreP in health and disease. These data reveal how hPreP's molecular features enable it to effectively recognize and degrade substrates in a manner that is flexible, eschewing strict requirements for substrate size, sequence, and physiochemical profile, yet specific, utilizing defined structural features to destroy amyloidogenic peptides.

EXPERIMENTAL PROCEDURES

HPreP Cloning, Expression, and Purification

HPreP cDNA was acquired from the Human ORFeome (Open Biosystems) and subcloned into an *E. coli* expression vector, pProEx, replacing its mitochondrial targeting sequence (aa 1–33) with an N-terminal - hexahistidine tag, which we refer to as WT. HPreP mutations were generated from this template using a Stratagene QuikChange site-directed mutagenesis kit and verified by sequencing. HPreP WT and E107Q were expressed in Rosetta(DE3) *E. coli* at 25°C with 300 μM isopropyl β-D-thiogalactopyranoside (IPTG) induction for 20 hr. HPreP mutants were induced with 30 μM IPTG for 8 hr at 20°C (Figures S1 and S3). Proteins were then purified over nickel-nitrilotriacetic acid affinity, Source Q anion exchange, and Superdex 200 gel filtration columns. Purified samples were flash-frozen in liquid nitrogen and stored at −80°C. Sample purity was assessed by SDS-PAGE (Figure S1).

Synthetic $A\beta_{40}$ Production

$A\beta_{40}$ was synthesized at a 0.25-mmol scale using fluorenylmethyloxycarbonyl chloride and *N,N,N′N′*-tetramethyl-*O*-(1H-benzotriazol-1-yl)uronium hexafluorophosphate/hydroxybenzotriazole chemistry on an Applied Biosystems 433A instrument. To increase peptide solubility and facilitate purification, we used a modified version of the method used by Sohma et al. (2004) as described in the Supplemental Experimental Procedures. $A\beta_{40}$ was purified by reverse phase high-performance liquid chromatography, lyophilized, and stored at −20°C under argon.

Protein Crystallization

To generate hPreP crystals, hPreP E107Q was subjected to reductive surface lysine methylation (KMe) after anion exchanger or gel filtration (Rypniewski et al., 1993) and then purified further by gel filtration. The initial condition was identified from high-throughput crystallization screens using commercially available kits and the Mosquito platform. Crystals were optimized for diffraction by precipitant, pH, buffer, and additive screening (Figure S1). Crystals were grown at 18°C by hanging drop vapor diffusion by combining 6 mg/ml KMe hPreP-E107Q in buffer containing 20 mM HEPES (pH 7.5), 250 mM NaCl, and 2 mM dithiothreitol, with the mother liquor containing 15.2% (w/v) polyethylene glycol 8,000, 15 mM Tris(2-carboxyethyl)phosphine, 80 mM sodium cacodylate (pH 6.5), 160 mM calcium acetate, and 20% (v/v) glycerol in a 1:1 (v/v) ratio. Within a week, crystals reached maximal size, ~0.1 mm in the longest dimension. To obtain the hPreP-Aβ complex, KMe hPreP E107Q was incubated with a 5 molar excess of $A\beta_{40}$ for 1 hour at 18°C, purified further by gel filtration, and crystallized as described above.

Data Collection and Structure Determination

Crystals were cryoprotected in mother liquor containing 30% (v/v) glycerol and then flash-frozen in liquid nitrogen. Diffraction data were collected at beamline

19ID at Argonne National Laboratory and processed using HKL3000 (Minor et al., 2006). A low-quality initial map (R_{free} = 48%) was obtained using a homology model of hPreP generated by I-TASSER (Roy et al., 2010) as a molecular replacement search model, followed by executing autobuild in PHENIX (Adams et al., 2010). The electron density map and refinement statistics were improved considerably by combining the phase information from MR with that derived from SAD using iodide as the heavy atom after briefly soaking the crystals in 200 mM potassium iodide for <30 s (Table 1; Figure S2). By inspection of the anomalous difference map, we discovered dimethylarsenic covalently bound to several cysteine residues (Figure S2) (Dyda et al., 1994). We took advantage of this to solve the Aβ-bound structure by MR/SAD using substrate-free hPreP as the search model and arsenic as the heavy atom (Table 1). Phasing and refinement were performed in PHENIX. Manual rebuilding and editing were done in COOT (Emsley and Cowtan, 2004). MolProbity (Chen et al., 2010) was used to validate stereochemistry.

Kinetic Assays

HPreP enzymatic activity was quantified at 37°C by monitoring the cleavage of substrate V (7-methoxycoumarin-4-yl-acetyl-RPPGFSAFK-2,4-dinitrophenyl, R&D Systems), a fluorogenic bradykinin mimetic, at an excitation wavelength of 327 nm and emission wavelength of 395 nm on a Tecan Safire microplate reader. To initiate the reaction, 1 μl 1.25 μM (125 pm) of hPreP was added to the various concentrations of substrate V in 50 mM KPO_4 (pH 7.3) to a final volume of 100 μl. Cleavage was assessed by measuring the fluorescence increase at 10-s intervals with 9 reads/well/time point. To determine the enzymatic activity, background subtraction and linear regression were used (R^2 cutoff = 97%). Specific activities (s^{-1}) were calculated by comparing the maximal fluorescence converted from the known quantity of substrate V by hPreP.

Aβ Degradation Assays

Aβ digestion reactions were performed at 37°C by adding 500 pmol $Aβ_{40}$ to 0.5–5 pmol of hPreP in a 10-μl reaction system. The reaction was quenched immediately (~1 s) by the addition of 10 μl stop solution (170 mM EDTA and 0.07% TFA). Samples were then reconstituted with 5μL 0.1% trifluoroacetic acid (TFA) and purified over a C_{18} column (Millipore). For MALDI-TOF/TOF analysis, samples were then mixed with 2.5 μl matrix (α-cyano-4hydroxycinnamic acid) in 70% acetonitrile (ACN) and 0.1% TFA and spotted onto the plate for data collection on an AB Sciex TOF/TOF 5800 machine in positive reflector or linear modes over 800–6,000 mass to charge ratio (m/z) range. Data were analyzed by MMass (Strohalm et al., 2010), fragments were matched with FindPept using a 0.5-Da tolerance, and b/y ions were identified with a molecular weight calculator. Q-TOF LC-MS/MS analysis used 1 pmol hPreP and 500 pmol $Aβ_{40}$. The reaction system was reconstituted with 10 μl 0.1% TFA, analyzed on an Agilent ChipCube II (300SB C_{18} Zorbax, 43 mm × 75 μm insertion device (ID), 5-μm particle size, 40-nl trapping column) by elution with 5–65% ACN over 8.0 min at 2.5 μl/min. Data were collected over 300–2,400 (m/z) on an Agilent 6540 Q-TOF LC-MS/MS machine in ESI+ mode and then analyzed and deconvoluted, b/y Ions identified, and fragments matched using a 30-ppm tolerance in MassHunter (Agilent).

SAXS Data Collection and Analysis

Data were collected at Argonne National Laboratory's Advanced Photon Source, beamline 18ID, at 23°C using a Mar 165 charge-coupled device (CCD) detector, an incident x-ray wavelength of 1.033 Å, and a protein concentration of 0.5 mg/ml. For Aβ binding experiments, hPreP was preincubated with a 2 molar excess of $Aβ_{40}$ for 20 min. Data were reduced using custom macros for IgorPro (WaveMetrics) written by the BioCAT staff and then analyzed using ATSAS (Petoukhov et al., 2012). We used PRIMUS and GNOM to determine the R_g in reciprocal and real space, respectively. Theoretical scattering curves were calculated for models and fit to the experimental data using CRYSOL, and OLIGOMER was used to determine the sample's percent composition by conformational state.

ACCESSION NUMBERS

The coordinates for the structures reported here have been deposited to the Protein Data Bank (http://www.pdb.org) with accession codes 4L3T (substrate-free hPreP) and 4NGE (Aβ-bound hPreP).

SUPPLEMENTAL INFORMATION

Supplemental Information includes Supplemental Experimental Procedures, six figures, two tables, and two 3D molecular models and can be found with this article online at http://dx.doi.org/10.1016/j.str.2014.05.003.

AUTHOR CONTRIBUTIONS

J.V.K., W.G.L., and W.J.T. designed and performed research and analyzed the data. K.P.S., A.B.S., and S.C.M. contributed reagents and data collection and analysis expertise. J.V.K. and W.J.T. wrote the paper.

ACKNOWLEDGMENTS

We are grateful to Lauren McCord, Raymond Hulse, and Adam Eisenberg for technical assistance and to Phoebe Rice for critical evaluation of experimental data. We thank the staff of SBC and BioCAT of the Advanced Photon Source at Argonne National Laboratory, operated by UChicago Argonne, LLC, for the U.S. Department of Energy, Office of Biological and Environmental Research under contract DE-AC02-06CH1135 for their help with data collection. This research was supported by the NIH (grants R01 GM81539 to W.J.T. and P41 GM103622 to BioCAT).

Received: December 28, 2013
Revised: April 12, 2014
Accepted: May 1, 2014
Published: June 12, 2014

REFERENCES

Abendroth, J., Gardberg, A.S., Robinson, J.I., Christensen, J.S., Staker, B.L., Myler, P.J., Stewart, L.J., and Edwards, T.E. (2011). SAD phasing using iodide ions in a high-throughput structural genomics environment. J. Struct. Funct. Genomics *12*, 83–95.

Adams, P.D., Afonine, P.V., Bunkóczi, G., Chen, V.B., Davis, I.W., Echols, N., Headd, J.J., Hung, L.W., Kapral, G.J., Grosse-Kunstleve, R.W., et al. (2010). PHENIX: a comprehensive Python-based system for macromolecular structure solution. Acta Crystallogr. D Biol. Crystallogr. *66*, 213–221.

Aleshin, A.E., Gramatikova, S., Hura, G.L., Bobkov, A., Strongin, A.Y., Stec, B., Tainer, J.A., Liddington, R.C., and Smith, J.W. (2009). Crystal and solution structures of a prokaryotic M16B peptidase: an open and shut case. Structure *17*, 1465–1475.

Alikhani, N., Berglund, A.K., Engmann, T., Spånning, E., Vögtle, F.N., Pavlov, P., Meisinger, C., Langer, T., and Glaser, E. (2011a). Targeting capacity and conservation of PreP homologues localization in mitochondria of different species. J. Mol. Biol. *410*, 400–410.

Alikhani, N., Guo, L., Yan, S., Du, H., Pinho, C.M., Chen, J.X., Glaser, E., and Yan, S.S. (2011b). Decreased proteolytic activity of the mitochondrial amyloid-β degrading enzyme, PreP peptidasome, in Alzheimer's disease brain mitochondria. J. Alzheimers Dis. *27*, 75–87.

Ashkenazy, H., Erez, E., Martz, E., Pupko, T., and Ben-Tal, N. (2010). ConSurf 2010: calculating evolutionary conservation in sequence and structure of proteins and nucleic acids. Nucleic Acids Res. *38*, W529–W533.

Baker, N.A., Sept, D., Joseph, S., Holst, M.J., and McCammon, J.A. (2001). Electrostatics of nanosystems: application to microtubules and the ribosome. Proc. Natl. Acad. Sci. USA *98*, 10037–10041.

Balbach, J.J., Ishii, Y., Antzutkin, O.N., Leapman, R.D., Rizzo, N.W., Dyda, F., Reed, J., and Tycko, R. (2000). Amyloid fibril formation by Aβ 16–22, a seven-residue fragment of the Alzheimer's β-amyloid peptide, and structural characterization by solid state NMR. Biochemistry *39*, 13748–13759.

Chen, V.B., Arendall, W.B., 3rd, Headd, J.J., Keedy, D.A., Immormino, R.M., Kapral, G.J., Murray, L.W., Richardson, J.S., and Richardson, D.C. (2010). MolProbity: all-atom structure validation for macromolecular crystallography. Acta Crystallogr. D Biol. Crystallogr. *66*, 12–21.

Chow, K.M., Gakh, O., Payne, I.C., Juliano, M.A., Juliano, L., Isaya, G., and Hersh, L.B. (2009). Mammalian pitrilysin: substrate specificity and mitochondrial targeting. Biochemistry *48*, 2868–2877.

Dyda, F., Hickman, A.B., Jenkins, T.M., Engelman, A., Craigie, R., and Davies, D.R. (1994). Crystal structure of the catalytic domain of HIV-1 integrase: similarity to other polynucleotidyl transferases. Science *266*, 1981–1986.

Emsley, P., and Cowtan, K. (2004). Coot: model-building tools for molecular graphics. Acta Crystallogr. D Biol. Crystallogr. *60*, 2126–2132.

Falkevall, A., Alikhani, N., Bhushan, S., Pavlov, P.F., Busch, K., Johnson, K.A., Eneqvist, T., Tjernberg, L., Ankarcrona, M., and Glaser, E. (2006). Degradation of the amyloid β-protein by the novel mitochondrial peptidasome, PreP. J. Biol. Chem. *281*, 29096–29104.

Farris, W., Mansourian, S., Chang, Y., Lindsley, L., Eckman, E.A., Frosch, M.P., Eckman, C.B., Tanzi, R.E., Selkoe, D.J., and Guenette, S. (2003). Insulin-degrading enzyme regulates the levels of insulin, amyloid β-protein, and the β-amyloid precursor protein intracellular domain in vivo. Proc. Natl. Acad. Sci. USA *100*, 4162–4167.

Guo, Q., Manolopoulou, M., Bian, Y., Schilling, A.B., and Tang, W.J. (2010). Molecular basis for the recognition and cleavages of IGF-II, TGF-α, and amylin by human insulin-degrading enzyme. J. Mol. Biol. *395*, 430–443.

Havugimana, P.C., Hart, G.T., Nepusz, T., Yang, H., Turinsky, A.L., Li, Z., Wang, P.I., Boutz, D.R., Fong, V., Phanse, S., et al. (2012). A census of human soluble protein complexes. Cell *150*, 1068–1081.

Huang, Y., and Mucke, L. (2012). Alzheimer mechanisms and therapeutic strategies. Cell *148*, 1204–1222.

Im, H., Manolopoulou, M., Malito, E., Shen, Y., Zhao, J., Neant-Fery, M., Sun, C.Y., Meredith, S.C., Sisodia, S.S., Leissring, M.A., and Tang, W.J. (2007). Structure of substrate-free human insulin-degrading enzyme (IDE) and biophysical analysis of ATP-induced conformational switch of IDE. J. Biol. Chem. *282*, 25453–25463.

Iwata, N., Tsubuki, S., Takaki, Y., Shirotani, K., Lu, B., Gerard, N.P., Gerard, C., Hama, E., Lee, H.J., and Saido, T.C. (2001). Metabolic regulation of brain Aβ by neprilysin. Science *292*, 1550–1552.

Johnson, K.A., Bhushan, S., Ståhl, A., Hallberg, B.M., Frohn, A., Glaser, E., and Eneqvist, T. (2006). The closed structure of presequence protease PreP forms a unique 10,000 Angstroms3 chamber for proteolysis. EMBO J. *25*, 1977–1986.

Kambacheld, M., Augustin, S., Tatsuta, T., Müller, S., and Langer, T. (2005). Role of the novel metallopeptidase Mop112 and saccharolysin for the complete degradation of proteins residing in different subcompartments of mitochondria. J. Biol. Chem. *280*, 20132–20139.

Koppen, M., and Langer, T. (2007). Protein degradation within mitochondria: versatile activities of AAA proteases and other peptidases. Crit. Rev. Biochem. Mol. Biol. *42*, 221–242.

Lu, J.X., Qiang, W., Yau, W.M., Schwieters, C.D., Meredith, S.C., and Tycko, R. (2013). Molecular structure of β-amyloid fibrils in Alzheimer's disease brain tissue. Cell *154*, 1257–1268.

Lustbader, J.W., Cirilli, M., Lin, C., Xu, H.W., Takuma, K., Wang, N., Caspersen, C., Chen, X., Pollak, S., Chaney, M., et al. (2004). ABAD directly links Aβ to mitochondrial toxicity in Alzheimer's disease. Science *304*, 448–452.

Malito, E., Hulse, R.E., and Tang, W.J. (2008). Amyloid β-degrading cryptidases: insulin degrading enzyme, presequence peptidase, and neprilysin. Cell. Mol. Life Sci. *65*, 2574–2585.

Manczak, M., Anekonda, T.S., Henson, E., Park, B.S., Quinn, J., and Reddy, P.H. (2006). Mitochondria are a direct site of Aβ accumulation in Alzheimer's disease neurons: implications for free radical generation and oxidative damage in disease progression. Hum. Mol. Genet. *15*, 1437–1449.

Manolopoulou, M., Guo, Q., Malito, E., Schilling, A.B., and Tang, W.J. (2009). Molecular basis of catalytic chamber-assisted unfolding and cleavage of human insulin by human insulin-degrading enzyme. J. Biol. Chem. *284*, 14177–14188.

McCord, L.A., Liang, W.G., Dowdell, E., Kalas, V., Hoey, R.J., Koide, A., Koide, S., and Tang, W.J. (2013). Conformational states and recognition of amyloidogenic peptides of human insulin-degrading enzyme. Proc. Natl. Acad. Sci. USA *110*, 13827–13832.

Minor, W., Cymborowski, M., Otwinowski, Z., and Chruszcz, M. (2006). HKL-3000: the integration of data reduction and structure solution—from diffraction images to an initial model in minutes. Acta Crystallogr. D Biol. Crystallogr. *62*, 859–866.

Moberg, P., Ståhl, A., Bhushan, S., Wright, S.J., Eriksson, A., Bruce, B.D., and Glaser, E. (2003). Characterization of a novel zinc metalloprotease involved in degrading targeting peptides in mitochondria and chloroplasts. Plant J. *36*, 616–628.

Moberg, P., Nilsson, S., Ståhl, A., Eriksson, A.C., Glaser, E., and Mäler, L. (2004). NMR solution structure of the mitochondrial F1β presequence from *Nicotiana plumbaginifolia*. J. Mol. Biol. *336*, 1129–1140.

Mossmann, D., Meisinger, C., and Vögtle, F.N. (2012). Processing of mitochondrial presequences. Biochim. Biophys. Acta *1819*, 1098–1106.

Mueller-Steiner, S., Zhou, Y., Arai, H., Roberson, E.D., Sun, B., Chen, J., Wang, X., Yu, G., Esposito, L., Mucke, L., and Gan, L. (2006). Antiamyloidogenic and neuroprotective functions of cathepsin B: implications for Alzheimer's disease. Neuron *51*, 703–714.

Murata, C.E., and Goldberg, D.E. (2003). *Plasmodium falciparum* falcilysin: a metalloprotease with dual specificity. J. Biol. Chem. *278*, 38022–38028.

Mzhavia, N., Berman, Y.L., Qian, Y., Yan, L., and Devi, L.A. (1999). Cloning, expression, and characterization of human metalloprotease 1: a novel member of the pitrilysin family of metalloendoproteases. DNA Cell Biol. *18*, 369–380.

Nilsson Cederholm, S., Bäckman, H.G., Pesaresi, P., Leister, D., and Glaser, E. (2009). Deletion of an organellar peptidasome PreP affects early development in *Arabidopsis thaliana*. Plant Mol. Biol. *71*, 497–508.

Olsen, J.V., Vermeulen, M., Santamaria, A., Kumar, C., Miller, M.L., Jensen, L.J., Gnad, F., Cox, J., Jensen, T.S., Nigg, E.A., et al. (2010). Quantitative phosphoproteomics reveals widespread full phosphorylation site occupancy during mitosis. Sci. Signal. *3*, ra3.

Paravastu, A.K., Leapman, R.D., Yau, W.M., and Tycko, R. (2008). Molecular structural basis for polymorphism in Alzheimer's β-amyloid fibrils. Proc. Natl. Acad. Sci. USA *105*, 18349–18354.

Petoukhov, M.V., Franke, D., Shkumatov, A.V., Tria, G., Kikhney, A.G., Gajda, M., Gorba, C., Mertens, H.D.T., Konarev, P.V., and Svergun, D.I. (2012). New developments in the ATSAS program package for small-angle scattering data analysis. J. Appl. Crystallogr. *45*, 342–350.

Pinho, C.M., Björk, B.F., Alikhani, N., Bäckman, H.G., Eneqvist, T., Fratiglioni, L., Glaser, E., and Graff, C. (2010). Genetic and biochemical studies of SNPs of the mitochondrial A β-degrading protease, hPreP. Neurosci. Lett. *469*, 204–208.

Porcelli, A.M., Ghelli, A., Zanna, C., Pinton, P., Rizzuto, R., and Rugolo, M. (2005). pH difference across the outer mitochondrial membrane measured with a green fluorescent protein mutant. Biochem. Biophys. Res. Commun. *326*, 799–804.

Powers, E.T., Morimoto, R.I., Dillin, A., Kelly, J.W., and Balch, W.E. (2009). Biological and chemical approaches to diseases of proteostasis deficiency. Annu. Rev. Biochem. *78*, 959–991.

Ralat, L.A., Kalas, V., Zheng, Z., Goldman, R.D., Sosnick, T.R., and Tang, W.J. (2011). Ubiquitin is a novel substrate for human insulin-degrading enzyme. J. Mol. Biol. *406*, 454–466.

Ravid, T., and Hochstrasser, M. (2008). Diversity of degradation signals in the ubiquitin-proteasome system. Nat. Rev. Mol. Cell Biol. *9*, 679–690.

Ren, M., Guo, Q., Guo, L., Lenz, M., Qian, F., Koenen, R.R., Xu, H., Schilling, A.B., Weber, C., Ye, R.D., et al. (2010). Polymerization of MIP-1 chemokine (CCL3 and CCL4) and clearance of MIP-1 by insulin-degrading enzyme. EMBO J. *29*, 3952–3966.

Roy, A., Kucukural, A., and Zhang, Y. (2010). I-TASSER: a unified platform for automated protein structure and function prediction. Nat. Protoc. *5*, 725–738.

Rypniewski, W.R., Holden, H.M., and Rayment, I. (1993). Structural consequences of reductive methylation of lysine residues in hen egg white lysozyme: an X-ray analysis at 1.8-A resolution. Biochemistry *32*, 9851–9858.

Saido, T., and Leissring, M.A. (2012). Proteolytic degradation of amyloid β-protein. Cold Spring Harb. Perspect. Med. *2*, a006379.

Sauer, R.T., and Baker, T.A. (2011). AAA+ proteases: ATP-fueled machines of protein destruction. Annu. Rev. Biochem. *80*, 587–612.

Shen, Y., Joachimiak, A., Rosner, M.R., and Tang, W.J. (2006). Structures of human insulin-degrading enzyme reveal a new substrate recognition mechanism. Nature *443*, 870–874.

Sohma, Y., Sasaki, M., Hayashi, Y., Kimura, T., and Kiso, Y. (2004). Design and synthesis of a novel water-soluble Aβ1–42 isopeptide: an efficient strategy for the preparation of Alzheimer's disease-related peptide, Aβ1–42, via O-N intramolecular acyl migration reaction. Tetrahedron Lett. *45*, 5965–5968.

Ståhl, A., Nilsson, S., Lundberg, P., Bhushan, S., Biverståhl, H., Moberg, P., Morisset, M., Vener, A., Mäler, L., Langel, U., and Glaser, E. (2005). Two novel targeting peptide degrading proteases, PrePs, in mitochondria and chloroplasts, so similar and still different. J. Mol. Biol. *349*, 847–860.

Strohalm, M., Kavan, D., Novák, P., Volný, M., and Havlícek, V. (2010). mMass 3: a cross-platform software environment for precise analysis of mass spectrometric data. Anal. Chem. *82*, 4648–4651.

Taylor, A.B., Smith, B.S., Kitada, S., Kojima, K., Miyaura, H., Otwinowski, Z., Ito, A., and Deisenhofer, J. (2001). Crystal structures of mitochondrial processing peptidase reveal the mode for specific cleavage of import signal sequences. Structure *9*, 615–625.

Tjernberg, L.O., Näslund, J., Lindqvist, F., Johansson, J., Karlström, A.R., Thyberg, J., Terenius, L., and Nordstedt, C. (1996). Arrest of β-amyloid fibril formation by a pentapeptide ligand. J. Biol. Chem. *271*, 8545–8548.

Voss, N.R., and Gerstein, M. (2010). 3V: cavity, channel and cleft volume calculator and extractor. Nucleic Acids Res. *38*, W555–W562.

Xia, D., Yu, C.A., Kim, H., Xia, J.Z., Kachurin, A.M., Zhang, L., Yu, L., and Deisenhofer, J. (1997). Crystal structure of the cytochrome bc1 complex from bovine heart mitochondria. Science *277*, 60–66.

Yankner, B.A., and Lu, T. (2009). Amyloid β-protein toxicity and the pathogenesis of Alzheimer disease. J. Biol. Chem. *284*, 4755–4759.